ACS OMEGA

Open Access

This article is licensed under CC-BY-NC-ND 4.0

http://pubs.acs.org/journal/acsodf

Article

CFD Simulation Investigation on the Flow Field Distribution Pattern under Different Operating Environment Pressures in a Jet Impingement-Negative Pressure Reactor

Yingying Dong, Facheng Qiu,* and Xinjie Chai

Cite This: *ACS Omega* 2024, 9, 1925−1935

Read Online

ACCESS | Metrics & More | Article Recommendations

ABSTRACT: A jet impingement-negative pressure deamination reactor (JI-NPDR) has excellent ammonia removal efficiency. The CFD numerical simulation method based on the Euler−Euler model and the realizable $k-\varepsilon$ turbulence model was used to investigate the effect of different negative pressures at the reactor top outlet on the distribution pattern of pressure, velocity, turbulent kinetic energy, and vortex. The results indicate that the overall water flow distribution in the reactor increases in axial cohesion with the increase in negative pressure. The scattered small eddies gradually connect to a large eddy current as a whole, and the small eddies generated in the jet area also become regular and flat with the increase of negative pressures. These findings can provide detailed information for the study of flow patterns in a jet impingement-negative pressure reactor.

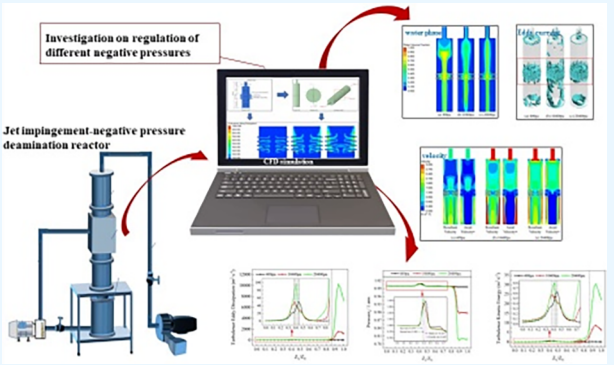

1. INTRODUCTION

In recent years, air stripping has been widely used in the treatment of high-concentration ammonia nitrogen wastewater.[1] In order to solve engineering practical problems such as scaling caused by the air stripping method, a negative pressure ammonia removal technology without air participation has been proposed and has good deamination efficiency. However, in the current research on negative pressure deamination, this technology requires a high vacuum degree of 70−100 kPa to maintain good ammonia removal efficiency, and there is a significant high energy consumption input.[2] Generally speaking, negative pressure deamination technology utilizes Henry's law equilibrium and the movement of ammonia nitrogen dissociation equilibrium to promote the release and transfer of ammonia.[3] From the perspective of enhancing mass transfer through the impact of porous jets, the jet impingement-negative pressure reactor was proposed to get a favorable deamination efficiency with a vacuum degree maintained at only 10−30 kPa.[4] The model of the jet and negative pressure is the point of coupled reinforcement techniques in the JI-NPDR, which results in a complex behavior within the flow field such as jet impingement, droplet atomization, cavitation, and so on. Thus, multiscale distribution characteristics within the flow field generated by pressure, velocity, turbulence, and disordered vortices are the core of JI-NPDR research.

Currently, the computational fluid dynamics (CFD) method is coupled with chemical experiments with the development of computer science and related applied technologies, which can describe the flow field in the reactor more explicitly. The representation of the kinematic properties of gas−liquid flow plays an important role in the research of the phase content, phase distribution, and phase characteristics in the flow field. Chang et al.[5,6] pointed out that CFD technology was used to study the negative pressure peeling of carbon dioxide in the liquid phase and found that the concentration of carbon dioxide in the parallel aggregation liquid stream was more concentrated. Peng et al.[7] used anisotropic droplets generated by negative pressure swirl to mix with air to enhance the flow effect of the flow field and promote dust settlement. In addition, Yan et al.[8] and Chen et al.[9] studied particles and the mixing characteristics of two-phase flow, respectively. In a word, these studies indicated that the flow field migration has an important influence on the distribution characteristics of fluids.

The pressure field can specifically describe the distribution, size, and change characteristics of pressure in the reactor. The pressure fluctuation under negative pressure has a significant effect on the heat and mass transfer behavior of the fluid. Liu et al.[10] confirmed that the pressure field generated by negative

Received: November 4, 2023
Revised: December 11, 2023
Accepted: December 13, 2023
Published: December 28, 2023

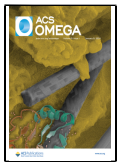

© 2023 The Authors. Published by American Chemical Society

https://doi.org/10.1021/acsomega.3c08692
ACS Omega 2024, 9, 1925−1935

pressure could affect the condensation of water vapor and the recovery of latent heat. Kim et al.[11] showed that the pressure fluctuation effect provided by different negative pressures could make the separation behavior of the gas phase different. The velocity field can express in detail the operation law of a variety of velocity vectors in the fluid, which provides an important basis for the evolution of the fluid flow state. Elghardouf et al.[12] modeled and analyzed the influence of negative pressure on airflow and found that a negative pressure difference could enhance the change of the air flow rate. Qiu et al.[13] used a deep learning framework to predict the velocity field of pumping thrusters, and they better demonstrated the change law of the jet velocity field. Local small eddies in the reactor easily produce waste of energy, and enhancing large eddies can enhance the dynamic mixing capacity of the fluid and increase the diffusion and mass transfer range. Chen et al.[14] used CFD technology and experiments to explore the gas−liquid vortex and found that the velocity and pressure had a greater influence on the vortex, and the vortex of the gas−liquid two-phase system could improve the efficiency of mass transfer. In addition, multiple velocity inlets could improve the uniformity and mixability of the velocity distribution. Combined with the research of Yi et al.,[15−17] it was found that a large vortex could enhance the homogenization micromixing ability of the liquid phase at the molecular scale and realize the rapid reaction and process strengthening between the gas−liquid phases of volatile organic compounds.

In addition, turbulent kinetic energy showed the instability of turbulent motion, revealed the chaotic degree of turbulence, showed the distribution and magnitude of turbulent energy of fluid flow, and was a concrete embodiment of fluid energy. The turbulent energy dissipation rate showed the efficiency of turbulent kinetic energy conversion to other energies, and it was greatly related to the pressure field and the velocity field and was the reference value of fluid energy conversion. The principal analysis of flow field, pressure and velocity, turbulent kinetic energy, and turbulent energy dissipation rate was studied.

In a word, in order to deepen the understanding of fluid motion mass transfer, this paper mainly carries out the investigation on the multiscale flow field distribution pattern of pressure, velocity, turbulent kinetic energy, and vortex in the new reactor. The CFD numerical simulation method based on the Euler−Euler model and realizable $k-\varepsilon$ turbulence model was used to investigate the effect of different negative pressures at the reactor top outlet. Meanwhile, the λ_2 eddy current criterion was also employed to explore the influence of different negative pressures on the vortex distribution pattern. The study will provide valuable guidance for the flow analysis and regulation of the JI-NPDR.

2. EXPERIMENTS AND METHODS

2.1. Governing Equations. The flow process of the fluid inside the reactor is controlled by the law of mass transfer, momentum transfer, and energy transfer, and its basic control equations are as follows:

Mass transfer equations

$$\frac{\partial \rho}{\partial t} + \nabla\cdot(\rho \boldsymbol{u}) = S_m \tag{1}$$

Momentum transfer equation

$$\frac{\partial(\rho u)}{\partial t} + \nabla\cdot(\rho u U) = -\frac{\partial p}{\partial x} + \mu\left(\frac{\partial^2 u}{\partial x^2} + \frac{\partial^2 u}{\partial y^2} + \frac{\partial^2 u}{\partial z^2}\right) + \rho f_x + s_x \tag{2}$$

$$\frac{\partial(\rho v)}{\partial t} + \nabla\cdot(\rho v U) = -\frac{\partial p}{\partial y} + \mu\left(\frac{\partial^2 v}{\partial x^2} + \frac{\partial^2 v}{\partial y^2} + \frac{\partial^2 v}{\partial z^2}\right) + \rho f_y + s_y \tag{3}$$

$$\frac{\partial(\rho w)}{\partial t} + \nabla\cdot(\rho w U) = -\frac{\partial p}{\partial z} + \mu\left(\frac{\partial^2 w}{\partial x^2} + \frac{\partial^2 w}{\partial y^2} + \frac{\partial^2 w}{\partial z^2}\right) + \rho f_z + s_z \tag{4}$$

Equation of energy transfer

$$\frac{\partial(\rho T)}{\partial t} + \nabla\cdot(\rho U T) = -\frac{\lambda}{c}\nabla^2 T + S_T \tag{5}$$

where $\boldsymbol{u}$ is the velocity vector and u, v, and w are velocity components in tangential, radial, and axial directions, respectively. S_m and S_T respectively represent the mass source term and energy source term. s_x, s_y, and s_z respectively represent components of the velocity source term. f_x, f_y, and f_z respectively represent the unit mass force of fluid micromasses in the direction of the three velocity vertical components. ρ is density. P is pressure. μ is dynamic viscosity. T is temperature. t is time. λ is thermal conductivity, and c is specific heat capacity.

2.2. Turbulence Model. The flow behavior of the fluid was divided into two states: laminar flow and turbulent flow. The change of state is affected by parameters such as velocity, pipeline physical properties, and fluid physical properties. In order to unify the judgment standard, Reynolds used the dimensionless Reynolds number Re to characterize and determine the state of the fluid[18]:

$$Re = \frac{\rho v d}{\mu} \tag{6}$$

where ρ is the density of the fluid. v is the average flow rate. d is the pipe diameter. μ is the dynamic viscosity.

The Reynolds mean (RANS) is the use of space-time averaging to deal with turbulence. It can reduce the calculation time cost while obtaining better results, and for most engineering projects, the details of turbulence fluctuations are often negligible.[19] RANS is more widely used in the range of indirect numerical simulation methods.

When solving for turbulence simulations using Reynolds averaging, the variables in the N−S equation (transfer of momentum) are often split into time average and pulsating components[20]:

Speed vector:

$$u = U + u' \tag{7}$$

Tangential velocity:

$$u = U + u' \tag{8}$$

https://doi.org/10.1021/acsomega.3c08692
ACS Omega 2024, 9, 1925−1935

Radial velocity:

$$v = V + v' \tag{9}$$

Axial speed:

$$w = W + w' \tag{10}$$

Pressure:

$$p = P + p' \tag{11}$$

It can be obtained by the time averaging of the basic control equations:

For incompressible fluids,

Continuity equation:

$$\text{div}\,\boldsymbol{U} = 0 \tag{12}$$

Reynolds mean equation:

$$\frac{\partial U}{\partial t} + \text{div}(U\boldsymbol{U}) = -\frac{1}{\rho}\frac{\partial P}{\partial x} + \boldsymbol{u}\text{div}(\text{grad}(U)) + \frac{1}{\rho}\left[\frac{\partial(-\overline{\rho u'^2})}{\partial x} + \frac{\partial(-\overline{\rho u'v'})}{\partial y} + \frac{\partial(-\overline{\rho u'w'})}{\partial z}\right] \tag{13}$$

$$\frac{\partial V}{\partial t} + \text{div}(V\boldsymbol{U}) = -\frac{1}{\rho}\frac{\partial P}{\partial y} + \boldsymbol{u}\text{div}(\text{grad}(V)) + \frac{1}{\rho}\left[\frac{\partial(-\overline{\rho u'v'})}{\partial x} + \frac{\partial(-\overline{\rho v'^2})}{\partial y} + \frac{\partial(-\overline{\rho v'w'})}{\partial z}\right] \tag{14}$$

$$\frac{\partial W}{\partial t} + \text{div}(W\boldsymbol{U}) = -\frac{1}{\rho}\frac{\partial P}{\partial z} + \boldsymbol{u}\text{div}(\text{grad}(W)) + \frac{1}{\rho}\left[\frac{\partial(-\overline{\rho u'w'})}{\partial x} + \frac{\partial(-\overline{\rho v'w'})}{\partial y} + \frac{\partial(-\overline{\rho w'^2})}{\partial z}\right] \tag{15}$$

Scalar transfer equation:

$$\frac{\partial \Phi}{\partial t} + \text{div}(\Phi\boldsymbol{U}) = \frac{1}{\rho}\text{div}(\Gamma_\Phi \text{grad}\,\Phi) + \left[-\frac{\overline{\partial u'\phi'}}{\partial x} - \frac{\overline{\partial v'\phi'}}{\partial x} - \frac{\overline{\partial w'\phi'}}{\partial x}\right] + S_\Phi \tag{16}$$

For compressible fluids,

Continuity equation:

$$\frac{\partial \overline{\rho}}{\partial x} + \text{div}(\overline{\rho}\tilde{\mathbf{U}}) = 0 \tag{17}$$

Reynolds mean equation:

$$\frac{\partial(\overline{\rho}\tilde{\mathbf{U}})}{\partial t} + \text{div}(\overline{\rho}\tilde{\mathbf{U}}\tilde{\mathbf{U}}) = -\frac{\partial \overline{P}}{\partial x} + \text{div}(\mu\ \text{grad}\ \tilde{\mathbf{U}}) + \left[-\frac{\partial(\overline{\rho u'^2})}{\partial x} - \frac{\partial(\overline{\rho u'v'})}{\partial y} - \frac{\partial(\overline{\rho u'w'})}{\partial z}\right] + S_{Mx} \tag{18}$$

$$\frac{\partial(\overline{\rho}\tilde{V})}{\partial t} + \text{div}(\overline{\rho}\tilde{V}\tilde{\mathbf{U}}) = -\frac{\partial \overline{P}}{\partial y} + \text{div}(\mu\ \text{grad}\ \tilde{V}) + \left[-\frac{\partial(\overline{\rho u'v'})}{\partial x} - \frac{\partial(\overline{\rho v'^2})}{\partial y} - \frac{\partial(\overline{\rho v'w'})}{\partial z}\right] + S_{My} \tag{19}$$

$$\frac{\partial(\overline{\rho}\tilde{W})}{\partial t} + \text{div}(\overline{\rho}\tilde{W}\tilde{\mathbf{U}}) = -\frac{\partial \overline{P}}{\partial z} + \text{div}(\mu\ \text{grad}\ \tilde{W}) + \left[-\frac{\partial(\overline{\rho u'w'})}{\partial x} - \frac{\partial(\overline{\rho v'w'})}{\partial y} - \frac{\partial(\overline{\rho w'^2})}{\partial z}\right] + S_{Mz} \tag{20}$$

Scalar transfer equation:

$$\frac{\partial(\overline{\rho}\tilde{\Phi})}{\partial t} + \text{div}(\overline{\rho}\tilde{\Phi}\tilde{\mathbf{U}}) = \text{div}(\Gamma_\Phi \text{grad}\ \tilde{\Phi}) + \left[-\frac{\overline{\partial(\overline{\rho}u'\phi')}}{\partial x} - \frac{\overline{\partial(\overline{\rho}v'\phi')}}{\partial x} - \frac{\overline{\partial(\overline{\rho}w'\phi')}}{\partial x}\right] + S_\Phi \tag{21}$$

After averaging in the N−S equation, it can be seen that there are three more normal stresses and three shear stresses in parentheses representing the time average variable. The unknown term described as $\overline{pu_i'u_j'}$ is the Reynolds stress term:

$$\tau_{ij}' = \overline{\rho u_i'u_j'} \tag{22}$$

In order to be able to calculate turbulence using the RANS equation, a new turbulence model equation needs to be established to close it.[21] Since there is a similarity between viscous stress and Reynolds stress on the average flow in the hypothetical view of fluid mechanics, stresses appear on the right side of the momentum equation, and in the viscosity law of Newton, the viscous stress is considered to be proportional to the deformation rate of the fluid element.[22] According to the vortex viscosity hypothesis,[23] the relationship between the two can be expressed linearly, and the Reynolds stress is expressed as a function of turbulent viscosity μ_t:

$$\tau_{ij} = -\overline{\rho u_i'u_j'} = \mu_t\left(\frac{\partial U_i}{\partial x_j} + \frac{\partial U_i}{\partial x_j}\right) - \frac{2}{3}\left(\rho K + \mu_t\frac{\partial U_i}{\partial x_I}\right)\delta_{ij} \tag{23}$$

https://doi.org/10.1021/acsomega.3c08692
ACS Omega 2024, 9, 1925−1935

$$k = \frac{1}{2}(\overline{u'^2} + \overline{v'^2} + \overline{w'^2}) \tag{24}$$

where K represents turbulent kinetic energy, δ_{ij} is the Kronecker symbol, and U_i represents the average velocity.

When the equation is closed, the Reynolds stress is linked to μ_t and μ_t can be expressed by an additional turbulence. The number of additional differential equations that must be solved corresponds to the number of additional turbulences. The RANS turbulence equation can be divided into the zero-equation, one-equation, two-equation, and multiequation models. The mixed-length model and the $k-\varepsilon$ model are currently the most widely used and effective.[24] The $k-\varepsilon$ model allows turbulence characteristics to be transmitted through convection and diffusion, and the description of turbulence is more complex, universal, and accurate. Moreover, the $k-\varepsilon$ model is more widely used, where the expression of k is shown in eq 24. The expression of ε is as follows:

$$\varepsilon = \frac{\mu}{\rho}\overline{\left(\frac{\partial U_i}{\partial x_j}\right)\left(\frac{\partial U_j}{\partial x_i}\right)} \tag{25}$$

There are three types of $k-\varepsilon$ models in Fluent: (standard) standard $k-\varepsilon$ models, (renormalized groups) RNG $k-\varepsilon$ models, and (achievable) realizable $k-\varepsilon$ models.[25] Compared with the previous two models, the realizable $k-\varepsilon$ model can better maintain the consistency of the Reynolds stress and real turbulence. The realizable $k-\varepsilon$ model has high accuracy in the fields of simulating swirl, diffusion, and jet, which is more in line with the changes of actual fluids.[26] So, in the turbulence model in this paper, the realizable $k-\varepsilon$ model was mainly selected for simulation description.

In the realizable $k-\varepsilon$ model, turbulent kinetic energy k, turbulent dissipation ε, and turbulent viscosity μ_t are expressed as follows:

Turbulent kinetic energy k:

$$\frac{\partial(\rho k)}{\partial t} + \frac{\partial(\rho k v_i)}{\partial x_i} = \frac{\partial}{\partial x_j}\left[\left(\mu + \frac{\mu_t}{\sigma_k}\right)\frac{\partial k}{\partial x_j}\right] + G_k + G_b - \rho\varepsilon - Y_M + S_k \tag{26}$$

Turbulent energy dissipation rate ε:

$$\frac{\partial(\rho\varepsilon)}{\partial t} + \frac{\partial(\rho\varepsilon v_i)}{\partial x_i} = \frac{\partial}{\partial x_j}\left[\left(\mu + \frac{\mu_t}{\sigma_\varepsilon}\right)\frac{\partial \varepsilon}{\partial x_j}\right] + \rho C_1 E\varepsilon - \rho C_2\frac{\varepsilon^2}{k + \sqrt{v\varepsilon}} + C_{1\varepsilon}\frac{\varepsilon}{K}C_{3\varepsilon}G_b + S_\varepsilon \tag{27}$$

Turbulent viscosity μ_t:

$$\mu_t = \rho C_\mu \frac{k^2}{\varepsilon} \tag{28}$$

where G_k and G_b are turbulent kinetic energy terms, $C_{1\varepsilon}$, C_2, and $C_{3\varepsilon}$ are empirical constants, C_μ is the turbulence coefficient, Y_M is the pulsating expansion term, σ_k and σ_ε are Prandtl numbers, and S_k and S_ε are source terms.

2.3. Multiphase Flow Model. The simulation of multiphase flow is mainly based on the Euler−Lagrange method and the Euler−Euler method. The former focuses on the simulation of the diffusion distribution of matter microelements in the continuous phase, and the latter focuses on the proportion and variable analysis between the two continuous flows.[27] So, the Euler−Euler method was used for the simulation calculation.

The mixture model has a wide range of applicability, high accuracy and variable processing accuracy for multiphase flow, and good stability. The multiphase flow mixture model is used to solve implicitly, ignoring the interphase slip velocity, and the basic control equation is as follows.

Mass conservation equation:

$$\frac{\partial}{\partial_t}(\rho_m) + \nabla\cdot(\rho_m \vec{u}_m) = 0 \tag{29}$$

$$\rho_m = \sum_{k=1}^{n} \alpha_k \rho_k \tag{30}$$

$$\vec{u}_m = \frac{\sum_{k=1}^{n} \alpha_k \rho_k \vec{u}_k}{\rho_m} \tag{31}$$

where ρ_m is the mixing density, $\vec{u}_m$ is the mass average velocity, α_k is the k-term volume fraction, and n is the total number of phases.

Momentum conservation equation:

$$\frac{\partial}{\partial_t}(\rho_m \vec{\nu}_m) + \nabla\cdot(\rho_m \vec{\nu}_m \vec{\nu}_m) = -\nabla p + \nabla\cdot[\mu_m(\nabla\vec{\nu}_m + \nabla\vec{\nu}_m^T)] + \rho_m\vec{g} + \vec{F} + \nabla\cdot(\sum_{k=1}^{n}\alpha_k\rho_k\vec{\nu}_{dr,k}\vec{\nu}_{dr,k}) \tag{32}$$

$$\mu_m = \sum_{k=1}^{n}\alpha_k\mu_k \tag{33}$$

$$\vec{\nu}_{dr,k} = \vec{\nu}_k - \vec{\nu}_m \tag{34}$$

μ_m is the mixed viscosity, $\vec{F}$ is the volume force, and $\vec{v}_{dr,k}$ is the drift velocity of the kth phase.

Equation of conservation of energy:

$$\frac{\partial}{\partial_t}\sum_{k=1}^{n}(\alpha_k\rho_k E_k) + \nabla\cdot\sum_{k=1}^{n}[\alpha_k\vec{\nu}_k(p + \rho_k E_k)] = \nabla\cdot k_{\text{eff}}\nabla T + S_E \tag{35}$$

where k_{eff} is the effective thermal conductivity and S_E is the other volumetric heat source.

Other phase volume fraction equations

$$\frac{\partial}{\partial_t}(\alpha_p\rho_p) + \nabla\cdot(\alpha_p\rho_p\vec{\nu}_m) = -\nabla\cdot(\alpha_p\rho_p\vec{\nu}_{dr,p}) + \sum_{q=1}^{n}(\dot{m}_{qp} - \dot{m}_{pq}) \tag{36}$$

where $\dot{m}_{qp}$ is the mass transfer from the q phase to the p phase and $\dot{m}_{pq}$ is the mass transfer from the q phase to the p phase.

2.4. Geometric Model and Boundary Conditions. The geometry shown in Figure 1 is shown in the geometric

https://doi.org/10.1021/acsomega.3c08692
ACS Omega 2024, 9, 1925−1935

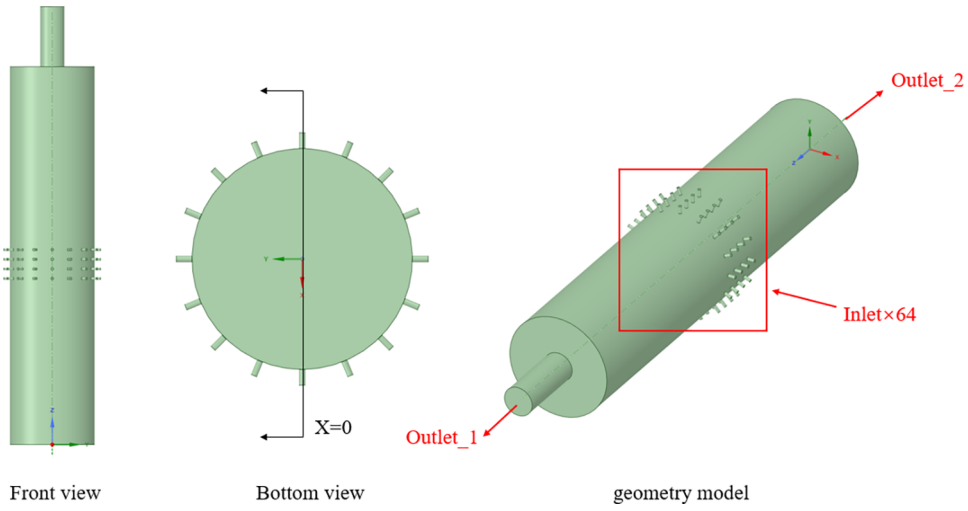

Figure 1. Reactor geometry diagram.

parameters shown in Figure 2. The model is constructed 1:1 with the reactor device, and each row has 16 equally spaced jet holes, a total of 4 rows, and a total of 64 holes.

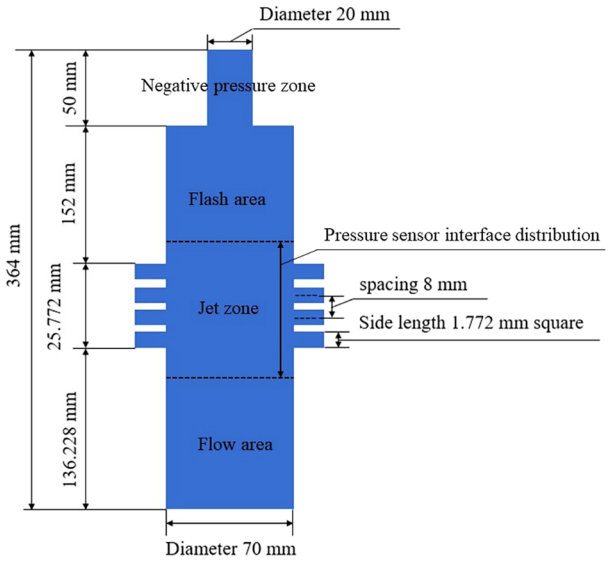

Figure 2. Reactor geometric parameters (X = 0 plane).

The slow flow zone is connected with the water tank to return the liquid. The jet area is connected with the inlet water pipe, and the liquid enters the 120 × 120 × 60 mm cube jacket through the water pipe and is evenly distributed. Moreover, the jet impact is carried out through the 2 mm small round holes evenly distributed on the wall of the main cylinder, with a total of 64 jet holes, 16 holes in a single row, and a total of 4 rows. The flash zone produces an atomization flash effect for gas–liquid separation. The negative pressure zone is connected to a vacuum pump to maintain the negative pressure while pumping outgas.

The fluid is represented by a two-phase flow model of Euler that compresses ideal gas (primary phase) and liquid water (secondary phase). The inlet boundary of the ring 64 hole adopts a speed inlet with a speed of 3 m/s. The liquid water volume fraction is 1, and the hydraulic diameter is 2 mm. The outlet boundary outlet_1 has a pressure outlet with gauge pressures of 400, 10,400, and 20,400 Pa (all negative), with a hydraulic diameter of 20 mm. The outlet boundary outlet_2 had a pressure outlet with a hydraulic diameter of 70 mm.

2.5. Validation of Grid Independence. Simulation was done using Fluent 3D double-precision and pressure-based transient solving (Figure 3). The simulation was carried out

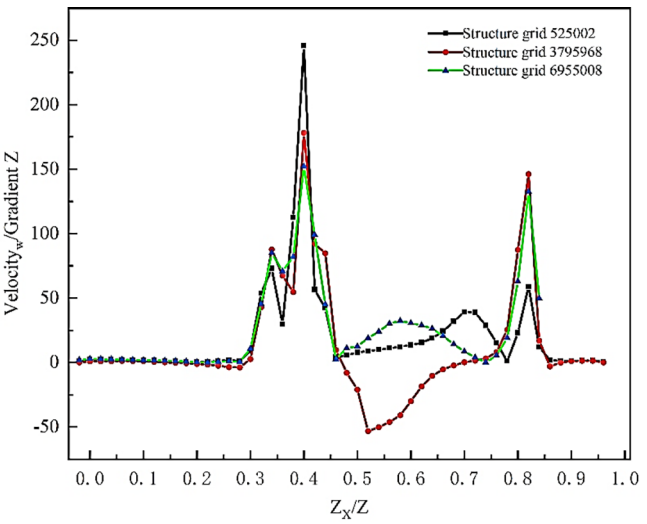

Figure 3. Grid-independent verification.

using the realizable k–ε turbulence model, scalable wall function, setting the operating pressure to 101,325 Pa, and coupled velocity and pressure solver. The pressure setting was the interpolation format. For accuracy, the second-order windward format was used, except for the volume change, which used the first-order windward format. Moreover, as the residual convergence was less than 10^{-3}, the average area weight of Z = 154 mm and Z = 162 mm plane pressure and velocity reached stability, and the inlet flow rate was stable; it was regarded as convergence.

3. RESULTS AND DISCUSSION

3.1. Jet Flow Field Analysis. As shown in Figure 4, the jet enters the reactor from a hole with an outer diameter of 2 mm and a length of 5 mm. After the central impact, the water flow

https://doi.org/10.1021/acsomega.3c08692
ACS Omega 2024, 9, 1925−1935

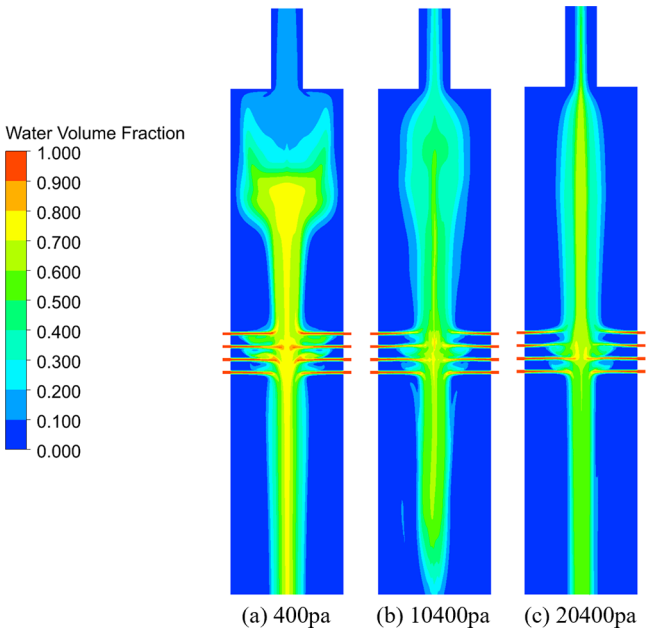

Figure 4. Cloud map of water phase distribution of the reactor under different negative pressures (X = 0 plane).

forms a more obvious liquid phase flow group in the jet area, which moves to the upper flash zone and the lower slow flow zone under the action of a negative pressure lifting force and gravity, showing impact symmetry. The negative pressures applied at the top of the reactor are 400, 10,400, and 20400 Pa, converted into absolute pressure values of 100,925, 90,925, and 80,925 Pa, respectively, and the rest are described by absolute pressure. Under the action of different negative pressures, the flow state change of the liquid phase has an obvious rule. With the increase of negative pressure, the axial cohesion of the overall water flow distribution in the reactor is enhanced.

Figure 5 shows that the axial action generated by the negative pressure lifting force and gravity mainly guides the

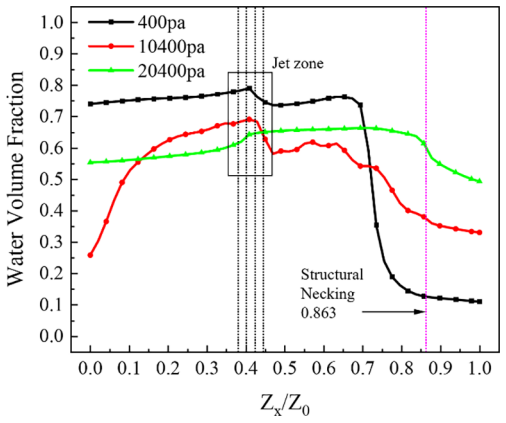

Figure 5. Variation curve of the water phase along the central axis of the reactor under different negative pressures.

movement of the water flow. The liquid film and droplets scattered in the flash zone, jet area, and slow flow area are small in volume and small in gravity. When the negative pressure is high, these scattered liquids undergo the process of aerodynamic fragmentation−coalescence−transfer. This results in a low water volume on both sides, coalescence of the water phase in the center, and an increased water volume at the neck of the structure. The falling liquid after the impact and extrusion in the jet zone maintains a high water volume and a high cohesive drop, resulting in a small change in the axial water volume along the Z-axis.

Figure 6 points out that the small vortices in the flash zone gradually disappear and the turbulent small vortices in the jet

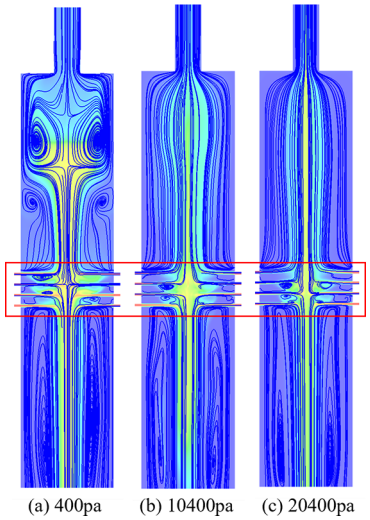

Figure 6. (a−c) Streamline trajectory of the reactor under different negative pressures (X = 0 plane).

zone remain in the process of increasing negative pressure. When the negative pressure is small, the impact of the fluid due to the traction of the air flow and air together in the flash area occurs with the formation of various types of small vortices. With the increase of negative pressure, fluid cohesion enhancement is caused by the gradual disappearance of small vortices in the flash area. The small vortex in the jet area will be present along with the jet flow all the time.

Figure 7 (left) shows that a jet with a negative pressure of 400 Pa impinges in the center and reduces the water volume by about 25%. Figure 7 (right) shows that the reductions in the water volume after central impingement were 30 and 35% for jets with negative pressures of 10,400 and 20,400 Pa, respectively. The radial velocity close to zero water flow clusters in the liquid after the impact to form a huge number of atomized droplets appears. The increase of negative pressure enhances the fragmentation effect of the jet and accelerates the rupture and transfer of the central stream mass. The upper part of the liquid accelerates toward the flash vapor zone, and the lower part of the liquid falls back toward the slow flow zone under the effect of gravity.

3.2. Pressure Field Analysis. Figure 8 shows the pressure profile varying along the reactor center axis r/R = 1, with the vertical coordinates indicating the ratio of the static absolute pressure value at each point to the standard atmospheric pressure of 101,325 Pa (1 atm = 101,325 Pa). It can be seen that in the jet zone, the point of impact for a negative pressure of 400 Pa is approximately near the third row of jet holes. The points of impact for negative pressures of 10,400 and 20,400 Pa are approximately near the second row of jet holes. As the negative pressure increases, the impingement center starts to shift from the third row of jet holes to the vicinity of the second row of jet holes. The increase of negative pressure at

https://doi.org/10.1021/acsomega.3c08692
ACS Omega 2024, 9, 1925−1935

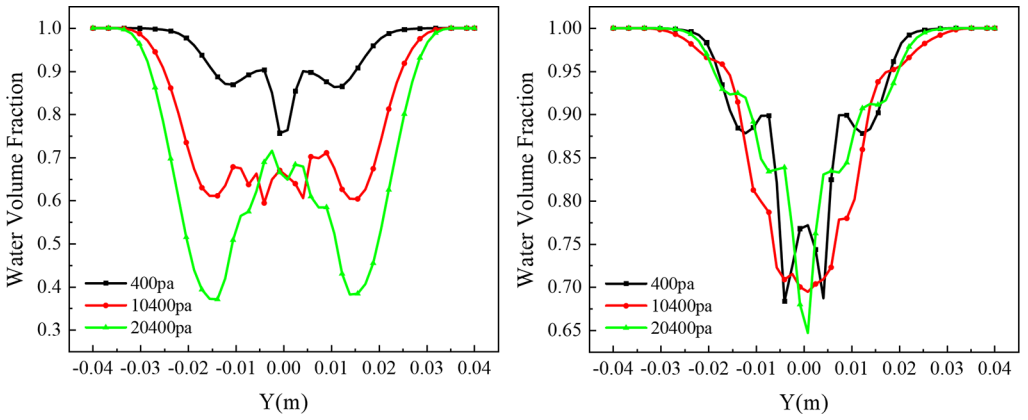

Figure 7. Variation curve of the water phase along the *y*-axis of the reactor under different negative pressures. Left: $x = 0$, $z = 154$ mm, i.e., the center of the third row of jet holes. Right: $x = 0$, $z = 146$ mm, i.e., the center of the second row of jet holes.

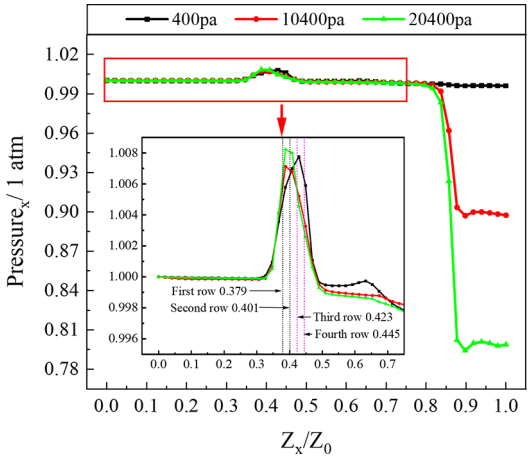

Figure 8. Variation curve of static pressure along the central axis of the reactor under different negative pressures.

the top causes the pressure weakening in the impingement zone to disperse, and the pressure weakening effect is more obvious the closer it is to the structural neck indentation.

Figure 9 shows that with the increase of negative pressure, the center pressure of the third row of jet holes gradually decreases, and the center pressure of the second row of jet holes increases. Moreover, the pressure core diffusion gradient gradually decreases. The weakening effect of negative pressure is the overall pressure of the third row of jets. The transfer effect and cohesion effect of negative pressure occur on the center of impingement of the water flow. The weakening effect of pressure dispersion along the *y*-axis from the center to the sides is observed in the case of overall reduction of the pressure core in the third row and in the case of the overall increase of the pressure core in the second row.

3.3. Velocity Field Analysis. As shown in Figures 10 and 11, the jet enters the reactor through a small hole at a speed of 3 m/s. After the impact effect occurs in the jet area, the main body of the flow group has a more obvious upward axial velocity and downward axial velocity to guide the water flow movement. The rest of the speed performance is mainly provided by the broken atomized droplets and air with strong fluidity. Through the comparison of the axial velocity of Figures 10 and 11, it can be seen that the negative pressure affects most of the area inside the reactor, it makes its internal substances have an upward movement speed. The gravitational influence range is limited, mainly to provide a downward movement speed for large and heavy liquid falling flow masses.

3.4. Turbulent Kinetic Energy Analysis. Figure 12 shows an overall increase in the average turbulent kinetic energy of the reactor with an increase in negative pressure, with the turbulent kinetic energy extremes in the jet region located near the point of impact and slightly shifted. Moreover, the turbulent kinetic energy extremes in the negative pressure region are close to the structure neck-down. Because of the

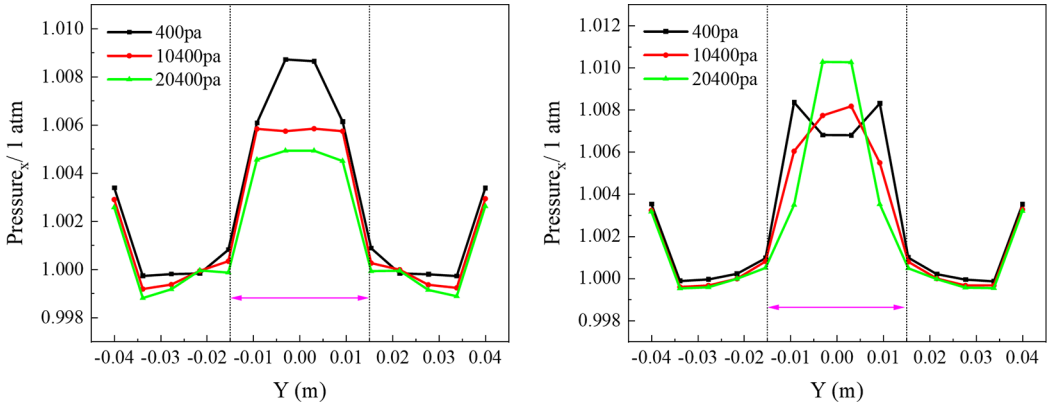

Figure 9. Variation curve of static pressure along the *y*-axis of the reactor under different negative pressures. Left: $x = 0$, $z = 154$ mm, i.e., the center of the third row of jet holes. Right: $x = 0$, $z = 146$ mm, i.e., the center of the second row of jet holes.

https://doi.org/10.1021/acsomega.3c08692
ACS Omega 2024, 9, 1925−1935

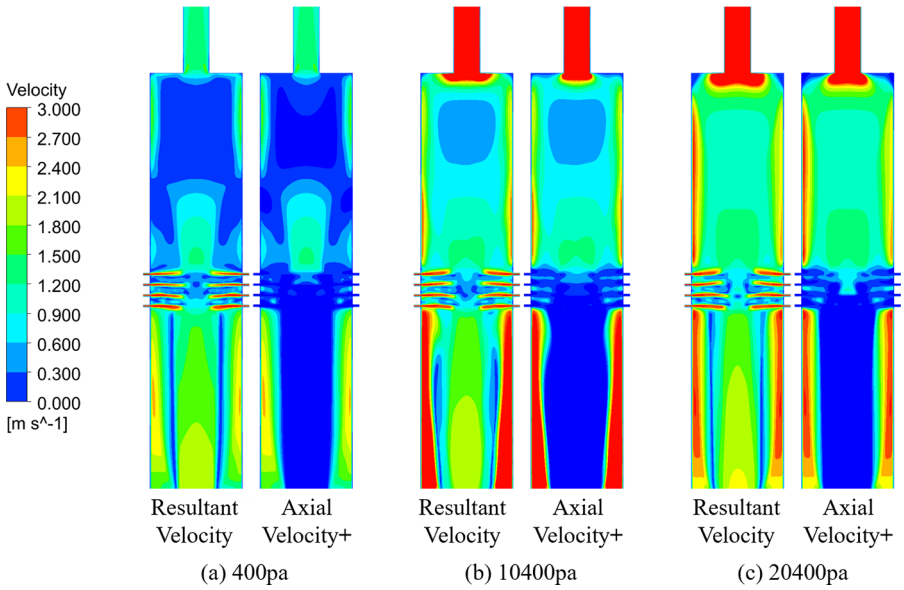

Figure 10. (a−c) Comparison of velocity distribution of the reactor under different negative pressures (X = 0 plane). Combined velocity on the left, axial velocity on the right, positive upward.

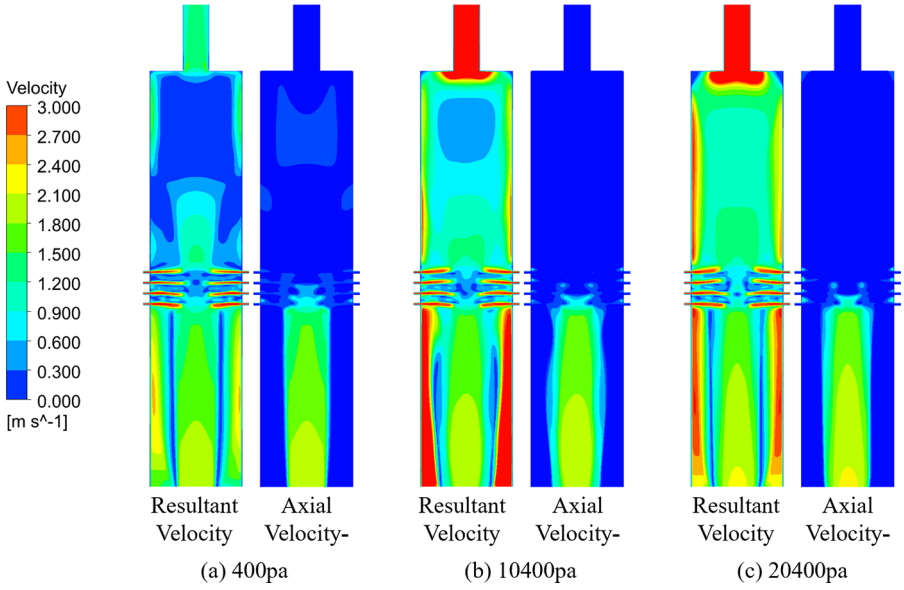

Figure 11. (a−c) Comparison of velocity distribution of the reactor under different negative pressures (X = 0 plane). Combined velocity on the left, axial velocity on the right, negative downward.

large central pressure generated during jet impingement, the turbulent chaos near the center of the impingement increases as a result. The turbulent kinetic energy poles are slightly shifted by the combined effect of pressure, velocity, and eddy currents, whereas the turbulent kinetic energy extremes in the negative pressure region are mainly generated by air flow. The negative pressure region in the reactor is subjected to the largest negative pressure gradient and value.

3.5. Turbulence Energy Dissipation Analysis. The turbulent kinetic energy dissipation rate shows the efficiency of the conversion of turbulent kinetic energy to other energies, which is a visual representation of energy transfer. Figure 13 shows that the turbulent kinetic energy generated by the jet is mainly distributed on both sides of the jet. As the jet surface is unstable, the oscillation crushing effect easily occurs under the influence of the outside world and provides a morphological basis for the exchange and transfer of energy. The increase in negative pressure injects additional energy into the longitudinal motion of the fluid and strengthens the velocity gradient and frictional shear. The turbulent kinetic energy dissipation rate at the impingement of the jet region is more obvious.

The overall increase in the average turbulent kinetic energy dissipation rate of the reactor with increasing negative pressure is demonstrated in Figure 14. The change in turbulent kinetic energy dissipation rate jet zone and negative pressure zone extremes from 400 to 10400 Pa on the center axis is relatively small, while the change in turbulent kinetic energy dissipation rate jet zone and negative pressure zone extremes from 10,400 to 20,400 Pa on the center axis is relatively large. As the negative pressure increases from 400 to 10,400 Pa, the effect of the increase in negative pressure on light fluids with a small volume and weight, such as droplets, liquid filaments, and air,

https://doi.org/10.1021/acsomega.3c08692
ACS Omega 2024, 9, 1925−1935

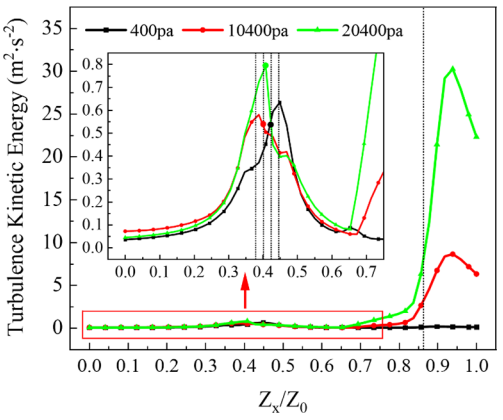

Figure 12. Change curve of turbulent kinetic energy along the central axis of the reactor under different negative pressures.

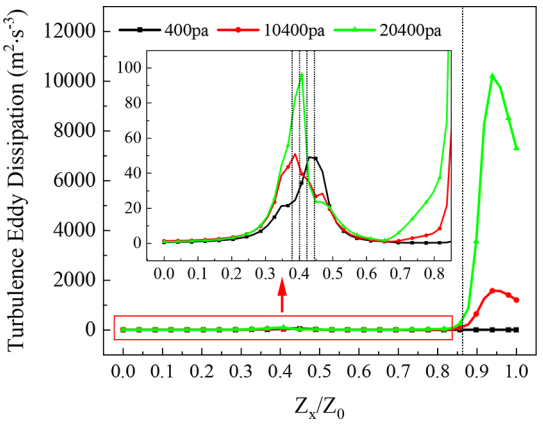

Figure 14. Change curve of the turbulent energy dissipation rate along the central axis of the reactor under different negative pressures.

is obvious to the extent that the extreme value of the negative pressure zone increases. Meanwhile, the jet area of the flow group has a certain weakening of the effect of the larger.

Figure 15 shows that with the negative pressure from 10,400 to 20,400 Pa, the negative pressure further increases. The liquid phase content of the center of the flow group is reduced, while the static pressure and turbulence energy gained are further increased. The liquid phase at this point in the jet zone appears to have a greater energy conversion effect. The liquid phase produced in the negative pressure zone due to aerodynamic fragmentation increases. The increase in the turbulent energy conversion of some of the liquid phases causes a large increase in the pole of the negative pressure zone.

3.6. Eddy Current State Analysis. In the reactor, the jet is often subjected to various transverse pressure effects perpendicular to the direction of fluid motion during radial motion, impingement mixing, negative pressure lifting, and gravity fallback. Moreover, the fluid velocity at the boundary layer is small and subject to large lateral pressure effects. Figure 16 shows with the increase in negative pressure, the vortex flow is restrained to some extent. The scattered small vortices are gradually linked into a whole large vortex flow. The further increase of negative pressure gradually integrates the disorganized vortices. The small vortices generated in the jet zone also flatten out regularly with the increase of negative pressure.

Figure 17 shows that the increase of the negative pressure gradually increases the distribution range and intensity of vortices. The largest vortices are concentrated in the jet region and the negative pressure region. As the increase in negative pressure accelerates the pressure drop in the reactor, this causes the pressure minima in the core of the small vortices to join together to form a larger vortex. The gradient of axial velocity gradually increases so that the small vortex follows the enhanced axial velocity to form a large vortex with a vertical structure, and the vortex structure is gradually ordered. The range and strength of the large vortex increase with the increase of axial velocity. The increase of negative pressure provides conditions for the whirlpool formation.

4. CONCLUSIONS

This section focuses on the effects of different ambient negative pressures on the parameters of the porous jet impingement-enhanced deamination process. The application of the CFD simulation platform was used to investigate the jet flow field, pressure, velocity, turbulence kinetic energy, turbulence kinetic energy dissipation rate, and vortex flow under different ambient negative pressures.

Negative pressure generated by the impact of the realization process was manifested in the increase in negative pressure. It accelerated the transformation of the central static pressure to the axial kinetic energy and made the axial velocity, gradient, and frictional sheer force of the water and air streams in the reactor increase. This led to the enhancement of aerodynamic fragmentation, the increase of airflow blowoff force, and the coalescence of the center of the water flow. The enhancement of the overall turbulent kinetic energy was an incidence, and the turbulent kinetic energy dissipation rate and a wider range

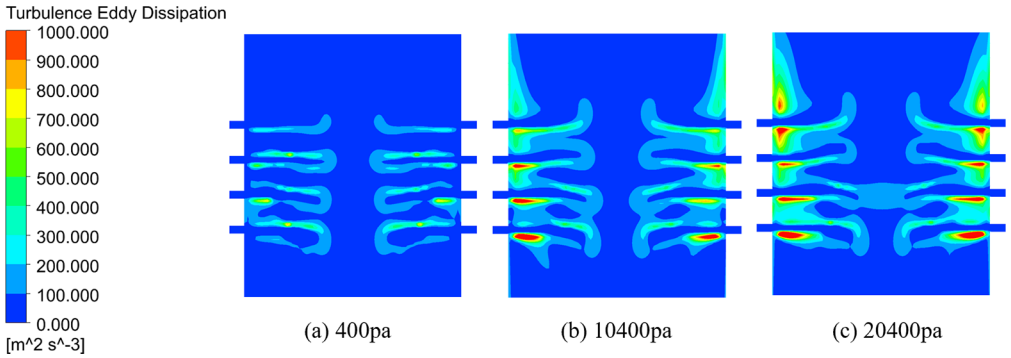

Figure 13. (a−c) Distribution of the turbulent energy dispersion rate in the jet area of the reactor under different negative pressures ($X = 0$ plane).

https://doi.org/10.1021/acsomega.3c08692
ACS Omega 2024, 9, 1925−1935

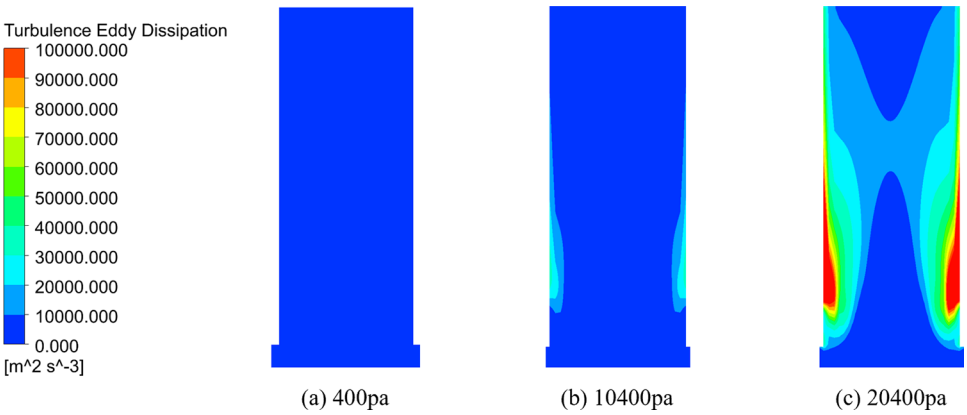

Figure 15. (a−c) Distribution of the turbulent energy dispersion rate in the negative pressure area of the reactor under different negative pressures (X = 0 plane).

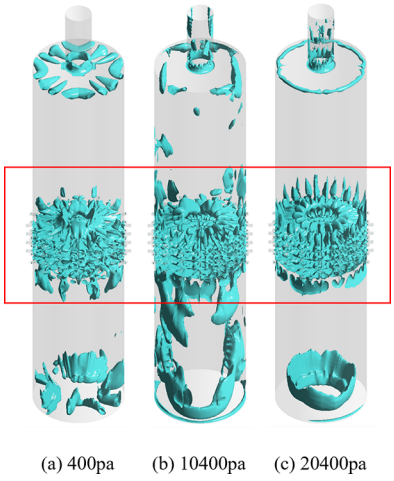

Figure 16. (a−c) Eddy current equivalence surface of the reactor under different negative pressures (λ_2 = −2000).

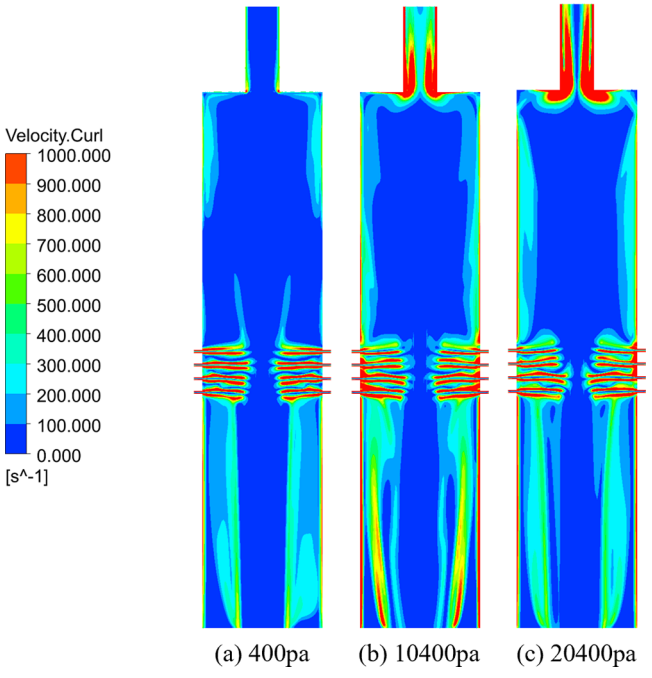

Figure 17. (a−c) Vortex cloud of the reactor under different negative pressures (X = 0 plane).

of distribution increased. The gradual linkage of small vortices and their normalization turned into large vortices.

AUTHOR INFORMATION

Corresponding Author

Facheng Qiu − *College of Chemistry and Chemical Engineering, Chongqing University of Technology, Chongqing 400050, China;* orcid.org/0000-0002-9998-9175; Email: qiufachengandl@126.com

Authors

Yingying Dong − *College of Chemistry and Chemical Engineering, Chongqing University of Technology, Chongqing 400050, China*

Xinjie Chai − *College of Chemistry and Chemical Engineering, Chongqing University of Technology, Chongqing 400050, China*

Complete contact information is available at: https://pubs.acs.org/10.1021/acsomega.3c08692

Notes

The authors declare no competing financial interest.

ACKNOWLEDGMENTS

The study was supported by the project of the Scientific Research Foundation of Chongqing University of Technology, Science and Technology Research Program of Chongqing Municipal Education Commission of China (KJQN202001112) and the Natural Science Foundation of Chongqing, China (cstc2021jcyj-msxmX0184).

REFERENCES

(1) Dai, M.; Quan, X.; Xu, F. Performance study of an arrayed straight-through channel packed tower for ammonia-nitrogen wastewater blowdown [J]. 2017, *31*(03), 90−96.

(2) Yellezuome, D.; Zhu, X.; Wang, Z. Mitigation of ammonia inhibition in anaerobic digestion of nitrogen-rich substrates for biogas production by ammonia stripping: A review. *Renewable Sustainable Energy Rev.* **2022**, *157*, 157.

(3) Keshavarz, M. H.; Rezaei, M.; Hosseini, S. H. A simple approach for prediction of Henry's law constant of pesticides, solvents, aromatic hydrocarbons, and persistent pollutants without using complex computer codes and descriptors[J]. *Process Safety and Environmental Protection* **2022**, *162*, 867−877.

(4) Qiu, F.; Quan, X.; Xiong, P. An ammonia nitrogen wastewater treatment device: ZL201911265243.7[P]. 2019-12−11.

https://doi.org/10.1021/acsomega.3c08692
ACS Omega 2024, 9, 1925−1935

(5) Chang, H.; Gan, H. Y.; Pan, R. H.; Ho, C. D. CFD Study of Hybrid Membrane Contactors for Absorption and Stripping of Carbon Dioxide. *Energy Procedia* **2017**, *105*, 4065−4071.
(6) Chang, H.; Gan, H.-Y.; Chen, Y.-H. Computational Fluid Dynamics Simulation Study of a Novel Membrane Contactor for Simultaneous Carbon Dioxide Absorption and Stripping. *Energies* **2017**, *10* (8), 1136.
(7) Peng, H.; Nie, W.; Zhang, S.; Cheng, W.; Liu, Q.; Guo, C.; Ma, Q.; Zhou, Z.; Xu, C.; Hua, Y.; Zhang, H. Research on negative pressure jet dust-removal water curtain technology for coal mine cleaner production. *Fuel* **2021**, *310*, 310.
(8) Yan, X.; Yao, Y.; Meng, S.; Zhao, S.; Wang, L.; Zhang, H.; Cao, Y. Comprehensive particle image velocimetry measurement and numerical model validations on the gas−liquid flow field in a lab-scale cyclonic flotation column. *Chem. Eng. Res. Des.* **2021**, *174*, 1−10.
(9) Chen, Z. B.; Yan, H. J.; Zhou, P.; Yang, P.; Ding, J. H.; Liu, J. Parametric study of gas−liquid two-phase flow field in horizontal stirred tank. *Trans. Nonferrous Met. Soc. China* **2021**, *31* (6), 1806−1817.
(10) Liu, Z.; Gao, Q.; Lu, X.; Ma, Z.; Zhang, H.; Wu, C. Experimental study of the optimal vacuum pressure in vacuum assisted air gap membrane distillation process. *Desalination* **2017**, *414*, 63−72.
(11) Kim, J.; Han, S. S.; Kim, J.; Lee, I. B.; Oh, H.; Yoon, Y. S. Vacuum pressure swing adsorption for efficient off-gas recycling: Techno-economic and CO2 abatement study. *Energy* **2023**, *264*, No. 126281.
(12) Elghardouf, N.; Lahlouh, I.; Elakkary, A.; Sefiani, N. Towards modelling, and analysis of differential pressure and air velocity in a mechanical ventilation poultry house: Application for hot climates. *Heliyon* **2023**, *9* (1), 129−136.
(13) Qiu, C.; Huang, Q.; Pan, G.; He, X. Multi-path deep learning framework on discrete pressure points to predict velocity field of pump-jet propulsor. *Appl. Ocean Res.* **2022**, *123*, 123.
(14) Chen, S.; Ouyang, Y.; Vandewalle, L. A.; Heynderickx, G. J.; Van Geem, K. M. CFD analysis on hydrodynamics and residence time distribution in a gas-liquid vortex unit. *Chem. Eng. J.* **2022**, *446*, 446.
(15) Yi, O.; Nunez, M. M.; Ruben, W.; et al. Liquid hydrodynamics in a gas-liquid vortex reactor. *Chem. Eng. Sci.* **2021**, *246*, No. 116970.
(16) Wang, M.; Joel, A. S.; Ramshaw, C.; Eimer, D.; Musa, N. M. Process intensification for post-combustion CO2 capture with chemical absorption: A critical review. *Appl. Energy* **2015**, *158*, 275−291.
(17) Falk, L.; Commenge, J. M. Performance comparison of micromixers[J]. *Chem. Eng. Sci.* **2010**, *65* (1), 405−411.
(18) Lodares, D.; Manzanero, J.; Ferrer, E.; Valero, E.; et al. An entropy−stable discontinuous Galerkin approximation of the Spalart−Allmaras turbulence model for the compressible Reynolds Averaged Navier−Stokes equations. *J. Comput. Phys.* **2022**, *455*, 455.
(19) Xiao, M.-J.; Yu, T.-C.; Ze, Y.-S.; et al. Physics-informed neural networks for the Reynolds-Averaged Navier−Stokes modeling of Rayleigh−Taylor turbulent mixing. *Comput. Fluids* **2023**, *266*, 266.
(20) Troldborg, N.; Sørensen, N. N.; Zahle, F. Immersed boundary method for the incompressible Reynolds Averaged Navier−Stokes equations. *Comput. Fluids* **2022**, *237*, 237.
(21) Romanelli, M.; Beneddine, S.; Mary, I.; et al. Data-driven wall models for Reynolds Averaged Navier−Stokes simulations. *Int. J. Heat Fluid Flow* **2023**, *99*, 99.
(22) Ali, A. E. A.; Afgan, I.; Laurence, D.; et al. A dual-mesh hybrid Reynolds-averaged Navier-Stokes/Large eddy simulation study of the buoyant flow between coaxial cylinders. *Nucl. Eng. Des.* **2022**, *393*, 393.
(23) Dong, Z.; Bürgler, M.; Hohermuth, B.; et al. Density-based turbulence damping at large-scale interface for Reynolds-averaged two-fluid models. *Chem. Eng. Sci.* **2022**, *247*, 247.
(24) Aydogdu, M. Analysis of the effect of rigid vegetation patches on the hydraulics of an open channel flow with Realizable k-ε and Reynolds stress turbulence models. *Flow Meas. Instrum.* **2023**, *94*, 94.
(25) Ishihara, T.; Qian, G.-W.; QI, Y.-H. Numerical study of turbulent flow fields in urban areas using modified k − ε model and large eddy simulation. *J. Wind Eng. Ind. Aerodyn.* **2020**, *206*, 206.
(26) Liu, Y.; Hinrichsen, O. Study on CFD−PBM turbulence closures based on k−ε and Reynolds stress models for heterogeneous bubble column flows. *Comput. Fluids* **2014**, *105*, 90−100.
(27) Suzuki, N.; Taura, D.; Komichi, Y. Critical micelle concentration and partition coefficient of mixed micelles: Analysis of ternary systems based on Markov chain model and simple mixture model. *J. Mol. Liq.* **2023**, *376*, 376.

https://doi.org/10.1021/acsomega.3c08692
ACS Omega 2024, 9, 1925−1935